Enhanced Resonant Tunneling in Symmetric 2D Semiconductor Vertical Heterostructure Transistors

Philip M. Campbell,[*,†,‡] Alexey Tarasov,[†] Corey A. Joiner,[†] William J. Ready,[‡] and Eric M. Vogel[†]

[†]School of Materials Science and Engineering and [‡]Georgia Tech Research Institute, Georgia Institute of Technology, Atlanta, Georgia 30332, United States

ABSTRACT Tunneling transistors with negative differential resistance have widespread appeal for both digital and analog electronics. However, most attempts to demonstrate resonant tunneling devices, including graphene—insulator—graphene structures, have resulted in low peak-to-valley ratios, limiting their application. We theoretically demonstrate that vertical heterostructures consisting of two identical monolayer 2D transition-metal dichalcogenide semiconductor electrodes and a hexagonal boron nitride barrier result in a peak-to-valley ratio several orders of magnitude higher than the best that can be achieved using graphene electrodes. The peak-to-valley ratio is large even at coherence lengths on the order of a few nanometers, making these devices appealing for nanoscale electronics.

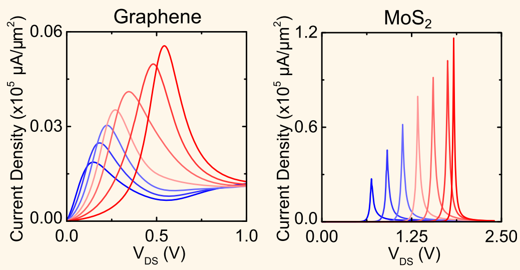

KEYWORDS: heterostructures · 2D materials · graphene · molybdenum disulfide · tunneling · resonance · negative differential resistance

Since the 1970s, resonant tunneling transistors have attracted significant attention for their potential in a variety of applications including low multivalued logic, high-frequency radar and communication systems, analog-to-digital conversion, and signal processing.[1] Devices such as the Esaki diode,[2−4] the resonant tunneling diode (RTD),[5−9] and the resonant tunneling transistor[10−12] have all been proposed. The defining property of these devices is negative differential resistance (NDR) in the current−voltage (*I*−*V*) characteristics. The presence of NDR creates a peak in the *I*−*V* characteristics that is defined by the ratio between the peak current and the current beyond the NDR region (valley current), known as the peak-to-valley ratio (PVR). However, despite intensive research efforts exploring a range of material systems, including Si/SiGe[7,8] and III−V quantum well systems,[5,9] the obtained PVR has been limited. A limited PVR degrades the performance of digital, high-frequency, and power systems with integrated resonant devices.[1,13,14]

The valley current in conventional 3D semiconductor resonant devices has three primary mechanisms. First, 3D semiconductor quantum wells have multiple longitudinal sub-bands due to quantization.[15] Each sub-band produces a distinct NDR peak, and the overlapping contributions to the current from each sub-band increase the valley current. Furthermore, the transverse dispersion relations for the sub-bands are typically not identical.[15,16] Therefore, at voltages above the primary resonance, the nonzero transverse momentum states of the sub-bands are more strongly coupled, increasing the number of tunneling channels that contribute to the current.[15,17] Second, the need for lattice matching during epitaxy limits the range of barrier materials and achievable band offset of the barrier. The lower band offset can result in thermionic emission, which contributes to the valley current.[17,18] Optimized AlGaN-based resonant devices with larger band offset barriers improve the valley current.[17] However, valley current in AlGaN is still limited by transport associated with higher sub-bands. Finally, the resonant states are effectively broadened due to a variety of possible scattering mechanisms. This broadening increases with energy so that the contribution of valley current due to higher sub-bands is enhanced.[16,17,19]

* Address correspondence to philip.campbell@gatech.edu.

Received for review December 16, 2014 and accepted April 29, 2015.

Published online April 29, 2015
10.1021/nn507174c

Vertical heterostructures consisting of two-dimensional (2D) materials such as graphene, hexagonal boron nitride (h-BN), and transition-metal dichalcogenides (TMDs) have a variety of properties that can potentially overcome some of the limitations of epitaxial 3D semiconductor heterostructures for resonant tunneling devices. 2D materials do not have additional longitudinal sub-bands that can contribute to valley current. Also, the van der Waals bonding between 2D materials in vertical heterostructures allows for a wider range of materials. For example, h-BN with a large band gap can be used for the tunneling barrier, limiting valley current associated with thermionic emission. Beyond the potential for improved performance, devices fabricated with 2D materials can be transferred to arbitrary substrates, permitting direct integration with other technologies such as in the back-end of a CMOS process.[20,21] Finally, the peak current of resonant devices depends exponentially on the barrier thickness, and the peak voltage depends on the quantization associated with nanometer thickness of the quantum wells. While molecular beam epitaxy of 3D semiconductors has matured to improve thickness control and uniformity, obtaining reproducible device characteristics still remains a challenge.[22] The lack of covalent bonding between layers of 2D materials can potentially lead to monolayer thickness control and improved reproducibility.

Recently, the graphene–insulator–graphene symmetric field effect transistor (symFET) has been proposed as a novel device exhibiting NDR.[23−26] For two identical (symmetric) 2D materials separated by an insulator, a peak in the tunneling current occurs when the transverse energy bands in one 2D material align completely with the other. The peak is a result of two mechanisms: (1) the entire density of states of both layers align, resulting in maximum overlap, and (2) the identical dispersion relations for the bands ensure a minimum of the difference in momentum of tunneling carriers (enhanced momentum conservation). As the bands become misaligned, the current decreases because the momentum difference of the tunneling carriers increases. For the graphene–insulator–graphene symFET, the resonant peak occurs approximately when the Dirac points of the graphene sheets align. Due to this interesting behavior, a great deal of recent theoretical and experimental work has explored the tunneling characteristics of vertical graphene–interlayer–graphene structures.[23−28] NDR behavior at room temperature has been demonstrated in devices that were carefully chosen to be free from contamination.[26] More recently, layered TMDs such as MoS_2[29] have received considerable attention due to their intriguing thickness-dependent electrical and optical properties and the presence of an intrinsic band gap.[30,31] Recent progress in large-area, uniform growth of MoS_2,[32,33] as well as controlled doping of MoS_2 devices,[34] brings more complex device geometries such as heterostructures within reach. Vertical stacks of different TMDs have been theoretically investigated,[35,36] predicting steep subthreshold swings. Surprisingly, negative differential resistance in vertical heterostructures consisting of TMDs has not been explored. In this work, symFETs incorporating TMDs as the electrodes are theoretically studied and compared to those having graphene electrodes. A strongly enhanced PVR in TMD heterostructures compared to graphene is observed due to the significant differences in the band structure of the materials.

RESULTS AND DISCUSSION

Figure 1 shows the device structure and band diagram of a 2D-to-2D symFET. Operation of the device relies upon tunneling between the top and bottom electrodes, composed of 2D materials, through a thin insulator. A voltage (V_{DS}) is applied to the top electrode relative to the bottom to align the bands. The top and bottom gates, V_{TG} and V_{BG}, are used to adjust the carrier concentrations in the layers. The relationships between the oxide voltages (V_{BOX}, V_{IOX}, and V_{TOX}), carrier concentrations, and terminal voltages are described in the Supporting Information.

Unlike previous reports that expressed the current density in wave-vector space,[24,25,35] we use an energy space formulation that is also derived using the Bardeen transfer Hamiltonian[37−39] as described in the Supporting Information. The energy space formulation permits a more natural energy band description of the differences in current–voltage characteristics between graphene and TMD symFETs.

The energy space equation for the current density is

$$J_{tot} = \frac{e|M_{B0}|^2}{\hbar}\int_E e^{-2\kappa d}\overbrace{g_B(E)g_T(E)}^{\alpha}\overbrace{(f_B - f_T)}^{\beta}\overbrace{\int_0^{2\pi} S_F(|\vec{q}|)d\theta}^{\gamma}dE \qquad (1)$$

where e is the electron charge and $\hbar$ is the reduced Planck's constant. $|M_{B0}|$ is a prefactor associated with the matrix element that describes the transfer of electrons between the electrodes. In the following simulations, we assume a value for this prefactor, as it affects only the magnitude of the current, not the shape of the current–voltage characteristic.[35] The exponential term in eq 1 captures the decay of the electron wave function upon tunneling through the barrier, where d is the interlayer thickness and κ is a decay factor. θ is the angular difference between the wave-vector of the tunneling carrier in the top and bottom layers. There are three portions of eq 1 that contribute to the shape of the tunneling current–voltage characteristics (labeled α, β, and γ in eq 1). Part α is the product of the density of states in the top ($g_T(E)$) and bottom layers ($g_B(E)$). To calculate the density of states, a parabolic dispersion relationship is assumed, which is valid for the energies involved in tunneling near the conduction

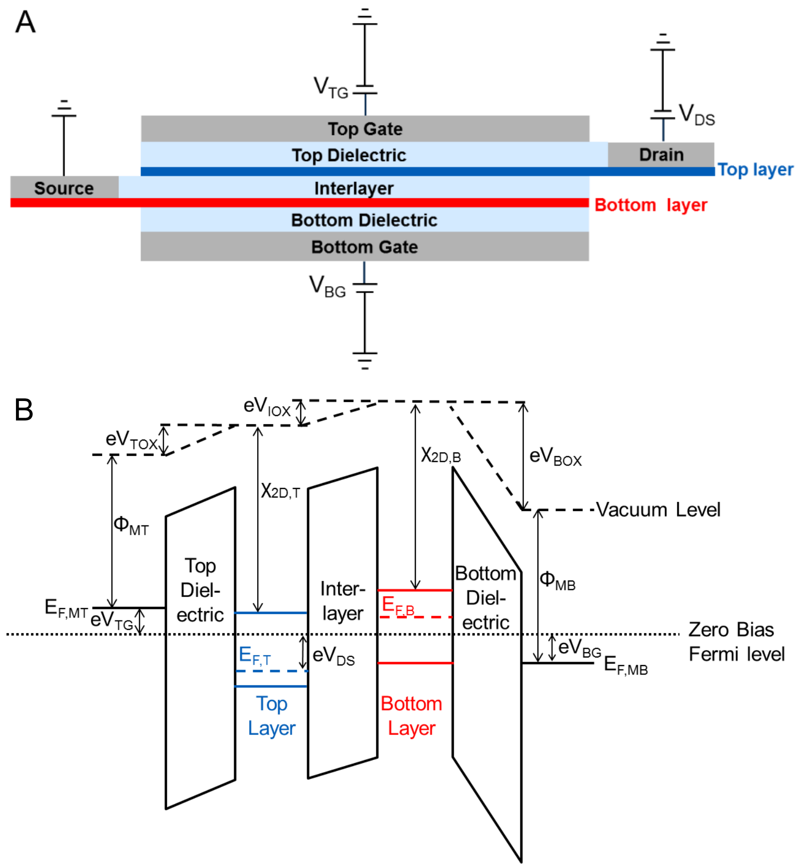

Figure 1. (A) SymFET device structure, consisting of two sheets of 2D materials separated by an interlayer tunneling dielectric. (B) Band diagram for the symFET with a negative top gate (V_{TG}) and positive bottom gate (V_{BG}) applied. These cause n- and p-type doping in the top and bottom layers, respectively. The applied source−drain bias (V_{DS}) controls the alignment between the band structures of the two layers to cause resonant tunneling. $E_{F,MT(MB)}$ represents the Fermi level of the top (bottom) gate, and $E_{F,T(B)}$ represents the Fermi level in the top (bottom) electrode. V_{IOX}, V_{BOX}, and V_{TOX} are the voltages across the interlayer, top, and bottom dielectrics, respectively. The dashed line represents the vacuum level, and the dotted line represents the zero bias Fermi level.

band minimum.[35] Part β, the difference between the two Fermi functions ($f_B - f_T$), sets a restriction on which of the overlapped states are available for tunneling, as electrons (holes) require an empty (filled) state to tunnel into. Part γ, $S_F(|\vec{q}|)$, represents the power spectrum of the scattering potential for tunneling carriers that depends on the magnitude of the difference in momentum of the top and bottom states ($|\vec{q}|$). One general form of this spectrum is given by

$$S_F(|\vec{q}|) = \frac{L_C^2}{\left[1+\left(\frac{|\vec{q}|}{q_C}\right)^2\right]^n} \qquad (2)$$

This form for $S_F(|\vec{q}|)$ arises due to short-range disorder within the material,[40,41] including electron−hole puddles causing potential fluctuations,[42] point defects, phonon scattering, and rotational misalignment between the 2D materials, creating moiré patterns.[43−45] Furthermore, while the calculation considers only elastic scattering, the form of this power spectrum is generally applicable to any scattering process. L_C is the coherence length,[24] which represents the lateral decay constant of disorder-induced scattering.[26,46] We assume that q_C and L_C are related by $L_C = q_C^{-1}$. For carriers in a structurally perfect 2D material with low scattering rate, L_C is the square root of the device area.[24] In the case of perfect rotational alignment between the top and bottom electrodes (see Supporting Information for the case of misalignment), $|\vec{q}|$ has the form

$$|\vec{q}| = (|k_T|\sin\theta)^2 + (|k_T|\cos\theta - |k_B|)^2 \qquad (3)$$

and describes the momentum difference between the starting and ending states, where $|k_T|$ and $|k_B|$ are the magnitude of the wave-vector in the top and bottom layers, respectively, and θ represents the angular difference between the states. The value of the exponent n in eq 2 depends on the detailed scattering mechanisms assumed and affects how quickly $S_F(|\vec{q}|)$ decays as the momentum difference increases. Recent theoretical simulations of 2D heterostructures have used n values of 1.5,[35,36] 2,[26] or 3.[24,25] In order to obtain a resonance peak, $S_F(|\vec{q}|)$ must decay as the difference in momentum ($|\vec{q}|$) increases,[26] which is the case for the form of $S_F(|\vec{q}|)$ given in eq 2, independent of the value

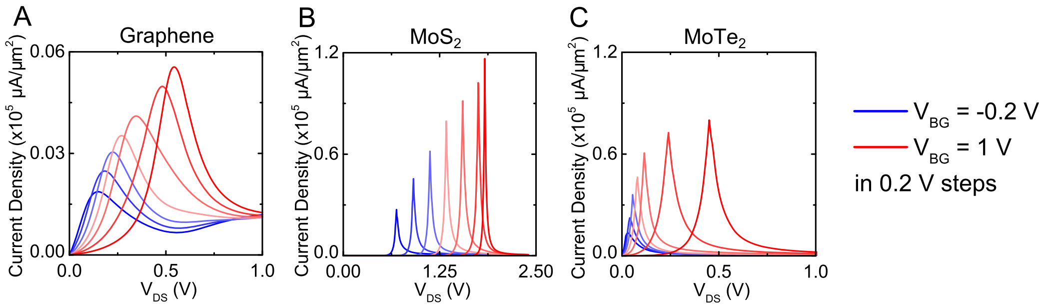

Figure 2. Simulated $J-V_{DS}$ characteristics for (A) graphene, (B) MoS_2, and (C) $MoTe_2$ symFETs. There is no doping in either layer of the devices. Each curve represents a different back-gate voltage, ranging from −0.2 to 1 V in 0.2 V steps. The top gate remains fixed at −1.5 V. The top and back gates are 4 layers of h-BN, with a capacitance of 3 μF/cm^2. The interlayer consists of two layers of h-BN (0.6 nm), with a capacitance of 6.2 μF/cm^2. We assume $|M_{B0}|$ = 0.01 eV, $\kappa = 3.8 \times 10^7$ cm^{-1}, n = 1.5, and $q_C^{-1} \approx 10$ nm.

for n assumed. While the value of n does affect the peak current density, peak width, and PVR, it does not change the overall trends observed in this paper.

Figure 2 compares the tunneling behavior of symFETs using graphene (A), MoS_2 (B), and $MoTe_2$ (C) as the top and bottom layers, with two layers (0.6 nm) of h-BN as the interlayer tunneling barrier. In each case, we consider equivalent top and bottom gate dielectrics with a capacitance of 3 μF/cm^2, and the top gate voltage is fixed at −1.5 V for each of the sweeps. Because there is a difference in the values of V_{TG} and V_{BG}, the carrier concentrations in the top and bottom layers are unequal. Therefore, at V_{DS} = 0 V, there is an offset between the band edges in the two electrodes, which we refer to as the zero bias offset.

For all three materials, the NDR peak shifts to higher V_{DS} values as the bottom gate voltage increases, depending on the zero bias offset between the top and bottom layers. Because the zero bias offset can be tuned by using the gate voltages to adjust the carrier concentrations, the location of the NDR peak is gate-tunable. As well, because the band gap determines the maximum value of the zero bias offset, it is expected that the position of the NDR peak will have a dependence on the band gap of the electrode material.

To examine the effect of the band gap on the NDR response of TMD symFETs, simulations were performed for $ZrSe_2$ and $HfSe_2$. To ensure equivalent electrostatic conditions for each material, the work functions of the top and bottom gates were adjusted for each material to ensure the same offset between the gate work functions and the conduction band of the material. Figure 3 shows the results of these simulations.

As predicted, decreasing the band gap of the TMD causes the NDR peak to shift to lower voltages. In these simulations, the gate conditions ensure that the top layer is p-type, while the bottom layer is n-type. As a result, the Fermi level in the top layer is near the valence band, while the Fermi level in the bottom layer is near the conduction band so that the zero bias offset is approximately equal to the value of the band gap. Consequently, the source−drain bias required to cause

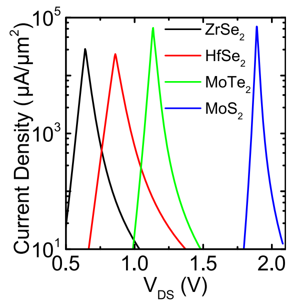

Figure 3. Simulated $J-V$ characteristics of $ZrSe_2$, $HfSe_2$, $MoTe_2$, and MoS_2. Simulations were performed with V_{TG} = −1.5 V, V_{BG} = 1.5 V, and $C_{TOX} = C_{BOX}$ = 3 μF/cm^2. The work functions of the top and back gates were adjusted for each material so that the difference between the gate work function and the conduction or valence band was equivalent. The interlayer consists of two layers of h-BN (0.6 nm), with a capacitance of 6.2 μF/cm^2. We assume $|M_{B0}|$ = 0.01 eV and $\kappa = 3.8 \times 10^7$ cm^{-1}.

alignment of the conduction and valence bands is lower for the materials with a smaller band gap.

In addition to the band gap effect, Figure 3 shows that the width of the NDR peak depends on the material. Specifically, MoS_2 has the narrowest peak, while $HfSe_2$ has the widest peak, due to the difference in the density of states in the materials. The density of states affects how quickly the current decays on the higher bias side of the NDR peak, causing a narrower peak in materials with a larger density of states. In addition, the density of states also affects the magnitude of the current density in symFETs (term α in eq 1). According to eq S8, the density of states in TMDs depends on the effective mass of charge carriers in the TMD. Therefore, the desired current−voltage response of symFETs can be tailored by choosing materials based on band gap and effective mass to determine the position and shape of the NDR peak.

Figure 4 shows the effect of coherence length on the tunneling current in graphene *versus* MoS_2 symFETs, with a value of V_{TG} = −1.5 V and V_{BG} = 1.5 V. Comparing the $J-V_{DS}$ characteristics with varying coherence lengths, it is clear there are two main differences between the two materials. First, for a given coherence length and value of n, there is a much higher PVR in

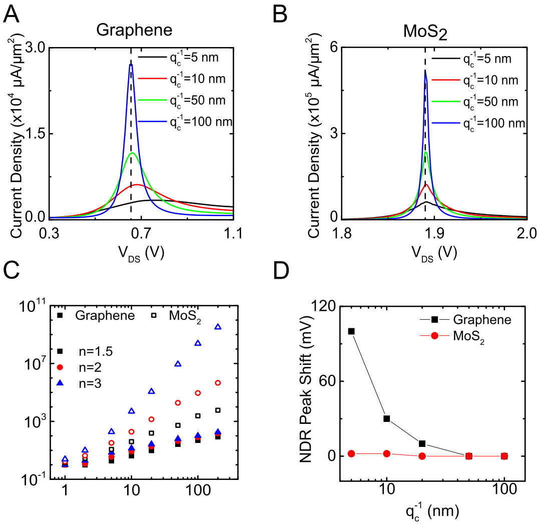

Figure 4. (A, B) Tunneling current density in graphene and MoS_2 with varying coherence lengths q_C^{-1}. (C) Comparison of the PVR dependence on coherence length in graphene and MoS_2 symFETs. Valley currents were measured 0.2 V above the NDR peak because the background current increases as a function of V_{DS}. (D) Comparison of the shift in NDR peak position (referenced to 100 nm value) at varying coherence lengths. There is almost no shift for MoS_2, while the graphene peak position has a large shift at small coherence lengths. Simulations were performed with $V_{TG} = -1.5$ V, $V_{BG} = 1.5$ V, and $C_{TOX} = C_{BOX} = 3\,\mu F/cm^2$. The interlayer consists of two layers of h-BN (0.6 nm), with a capacitance of 6.2 $\mu F/cm^2$. We assume $|M_{B0}|$ = 0.01 eV and $\kappa = 3.8 \times 10^7$ cm^{-1}.

MoS_2 than in graphene. At large coherence lengths, the PVR in MoS_2 approaches 10^9, while the PVR in graphene is limited to a few hundred. The NDR peak in MoS_2 is present at smaller coherence lengths than in graphene, suggesting that MoS_2 symFETs could be scaled to smaller device sizes than graphene symFETs. Second, at small coherence lengths, the voltage at which the peak occurs for graphene shifts significantly, whereas the peak in MoS_2 shifts minimally.

To further explain the differences in behavior for TMD symFETs compared to graphene symFETs, we explore how each of the components of the tunneling current changes as a function of source−drain bias (terms α, β, and γ in eq 1). First, we consider the case of graphene. Figure 5A−C compares the density of states (dashed lines) and Fermi level difference (solid line) contributions to the graphene tunneling current for source−drain bias conditions less than the peak (A), at the peak (B), and greater than the peak (C). The dark shaded areas in each graph represent the density of states at each energy that are available for tunneling (the product of the α and β terms in eq 1). As the source−drain bias increases, the dark shaded area in Figure 5A−C increases nonlinearly, causing the background current to increase nonlinearly.

Figure 5D−F show the evolution of $S_F(|\vec{q}\,|)$ with source−drain bias for graphene (black curve). The red-shaded area represents the current density at a

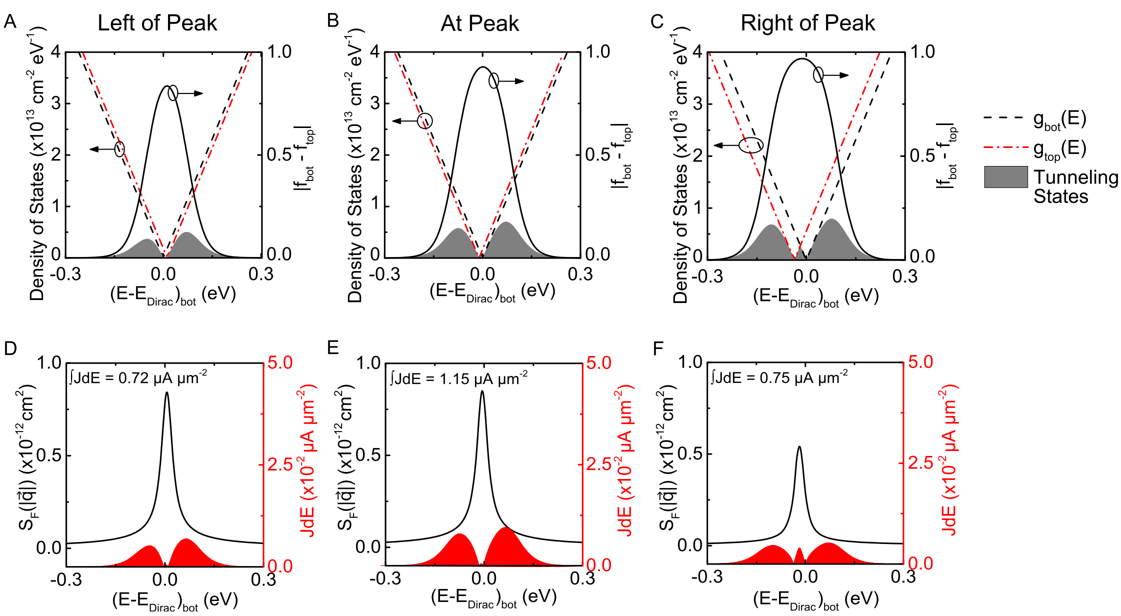

Figure 5. Different contributions to the tunneling current in graphene symFETs. (A−C) Density of states of the top (g_{top}) and the bottom layer (g_{bot}) and the Fermi function overlap of both layers ($|f_{bot} - f_{top}|$) *versus* the energy, referenced to the bottom layer Dirac point. The dark shaded area shows the portion of states capable of tunneling. (D−F) Spectrum of the scattering potential (solid line, left axis) and the contribution to the current density at each energy (red shaded area, right axis). The integral of the red-shaded area ($\int JdE$) gives the current density at a given bias voltage. (A, D) At low source−drain voltages, there is a small overlap between the Fermi functions in an area with low densities of states and a small value of $S_F(|\vec{q}\,|)$, causing a low tunneling current. (B, E) As the source−drain voltage reaches the NDR peak, the contribution due to band alignment grows and there is a high probability of tunneling, causing the current to reach a maximum. (C, F) Increasing the source−drain voltage increases the band alignment contribution but decreases the probability of tunneling, causing the current to decrease. Simulations were performed with $V_{TG} = -1.5$ V, $V_{BG} = 1.5$ V, and $C_{TOX} = C_{BOX} = 3\,\mu F/cm^2$. The interlayer consists of two layers of h-BN (0.6 nm), with a capacitance of 6.2 $\mu F/cm^2$. We assume $|M_{B0}|$ = 0.01 eV, $\kappa = 3.8 \times 10^7$ cm^{-1}, $n = 1.5$, and $q_C^{-1} \approx 10$ nm.

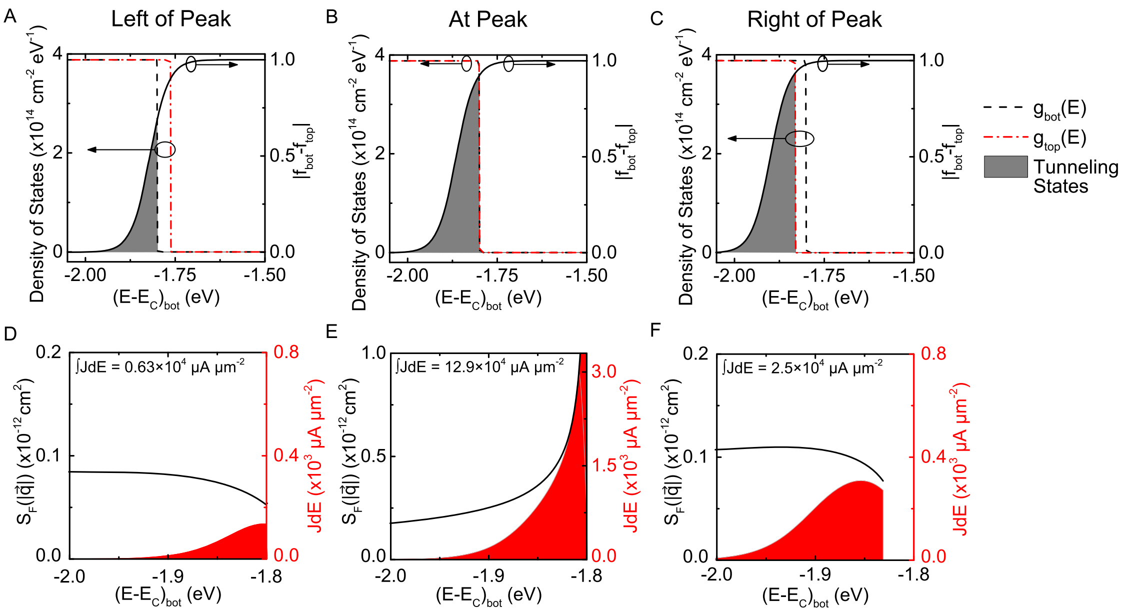

Figure 6. Different contributions to the MoS_2 tunneling current at three source−drain bias conditions. (A−C) Density of states of the top (g_{top}) and the bottom layer (g_{bot}) and the Fermi function overlap of both electrodes ($|f_{bot} - f_{top}|$) *versus* the energy referenced to the bottom layer conduction band. The dark shaded area shows the portion of states capable of tunneling. (D−F) Spectrum of the scattering potential (solid line, left axis) and the contribution to the current density at each energy (red-shaded area, right axis). The integral of the red-shaded area ($\int JdE$) gives the current density at a given bias voltage. (A, D) At low source−drain voltages, there is a small overlap between the Fermi functions, and the density of states in the MoS_2 with the area limited by the band edge of the bottom layer. $S_F(|\vec{q}|)$ also has small values in the range where tunneling can occur. (B, E) The band edges perfectly align at the NDR peak, with a larger contribution from the density of states and Fermi function overlap and a maximum probability of tunneling. (C, F) As V_{DS} continues to increase, the only increase in the states that can tunnel comes from small changes in the Fermi level due to increases in carrier concentrations. The probability of tunneling is small for most energies and the range of energies over which tunneling can occur is cut off by the top layer band edge, leading to a small valley current. Simulations were performed with $V_{TG} = -1.5$ V, $V_{BG} = 1.5$ V, and $C_{TOX} = C_{BOX} = 3\ \mu F/cm^2$. The interlayer consists of two layers of h-BN (0.6 nm), with a capacitance of 6.2 $\mu F/cm^2$. We assume $|M_{B0}| = 0.01$ eV, $\kappa = 3.8 \times 10^7\ cm^{-1}$, $n = 1.5$, and $q_C^{-1} \approx 10$ nm.

given E (the product of terms α, β, and γ in eq 1), with the total current density given by the integral of the red-shaded area. When the Dirac points in the two electrodes are not aligned, there is a single energy where the magnitude of the wave-vector in the top layer and the magnitude of the wave-vector in the bottom layer are equivalent and a small range of energies where the momentum difference is small enough that there is still a high probability of tunneling. For most values of energy, there is a large wave-vector difference and the probability of tunneling is small. Because tunneling can occur only for a narrow range of energies, the current density is also small. In contrast, at the NDR peak (Figure 5E) there is a small difference in the magnitude of the wave-vector and high tunneling probability for all energies. At a given coherence length, as V_{DS} changes, the Dirac points of the two graphene layers move gradually relative to one another and the product of terms α, β, and γ of eq 1 increases to a maximum at the NDR peak before decreasing again. The smooth transition for graphene is due to the linearly increasing density of states as a function of energy. As the coherence length decreases, the width of the $S_F(|\vec{q}|)$ function increases. Because the density of states and Fermi function difference (eq 1 terms α and β) are always increasing as a function of source−drain bias and the current density depends on the product of $S_F(|\vec{q}|)$ with these terms, the NDR peak position is a function of coherence length (Figure 4D).

In 2D TMDs such as MoS_2 and $MoTe_2$, the characteristics of the NDR peak are significantly altered by the differences in band structure compared to graphene. The theoretical density of states for TMDs is constant within the valence and conduction bands, with zero states available within the band gap. Because tunneling can occur only at points where both densities of states are nonzero, tunneling is restricted to two energy ranges: one within the conduction band and the other within the valence band.

To the left of the resonance peak, only a small number of states can tunnel, governed by the tail of the Fermi functions in each layer (solid line in Figure 6A). As the bias voltage increases, the band edges move closer together and more of the Fermi function difference overlaps with the density of states, causing large increases in the tunneling current with small changes in bias voltage. The NDR peak occurs at the V_{DS} where the band edges of the TMD layers are aligned (Figure 6B). To the right of the resonance peak, the contribution from the density of states (term α in eq 1) is constant and the current changes only due to the Fermi level (Figure 6C). This suppresses the valley current and contributes to the increased PVR observed in TMD symFETs.

Figure 6D−F shows $S_F(|\vec{q}|)$ for MoS_2 to MoS_2 tunneling. At source−drain values far from the resonance

ARTICLE

TABLE 1. Comparison of PVR in Different Types of Resonant Tunneling Structures

ref	materials	q_c^{-1} (nm)	n	T (K)	PVR	V_{DS} at peak position (V)
5	InGaAs/AlAs/InAs			300	30	1.94
7	Si/SiGe			300	2.43	2
9	GaSb/AlSb/InAs			77	2.7	
17	GaN/AlGaN (theory)				455	7.5
15	InGaAs/InAlAs (theory)				20	0.4
26	graphene-h-BN-graphene (expt)			7	4	0.32
				300	1.3	1
26	graphene-h-BN-graphene (theory)	12	2	10	4	0.3
25	graphene-h-BN-graphene (theory)	12	3	10	10	0.28
this paper	graphene-h-BN-graphene (theory)	10	3	300	14	0.68
		200	3	300	180	
this paper	MoS_2-hBN-MoS_2 (theory); $E_G = 1.8$ eV; $m_e^* = 0.378$	10	3	300	4854	1.9
		200	3	300	10^9	
this paper	$MoTe_2$-hBN-$MoTe_2$ (theory); $E_G = 0.9$ eV; $m_e^* = 0.235$	10	3	300	1041	1.14
		200	3	300	3×10^8	
this paper	$HfSe_2$-hBN-$HfSe_2$ (theory); $E_G = 0.45$ eV; $m_e^* = 0.18$	10	3	300	114	0.86
		200	3	300	1.8×10^8	
this paper	$ZrSe_2$-hBN-$ZrSe_2$ (theory); $E_G = 0.29$ eV; $m_e^* = 0.22$	10	3	300	296	0.64
		200	3	300	2×10^8	

peak, the tunneling probability is small, resulting in low values of valley current. Near the band edge, $S_F(|\vec{q}|)$ decreases due to the $\sqrt{E}$ dependence of the momentum in each layer. Far from the band edge, the change in wave-vector with energy is small so that the difference between the magnitude of the wave-vectors ($|\vec{q}|$) of each layer is constant. When the band edges are offset, the magnitude of the wave-vector near the band edge producing the cutoff varies more quickly than in the other layer, causing a larger difference in momentum between the top and bottom layers. At the resonance peak, the contribution from $S_F(|\vec{q}|)$ enters the peaked region and the decrease in $S_F(|\vec{q}|)$ near the band edge disappears because the band edges are aligned and the momentum difference is a minimum. This results in a steep, narrow peak in the current–voltage characteristic.

An important consideration for the fabrication of real devices is the effect that band tail states will have on the current–voltage characteristic. In currently available synthetic 2D materials, the large number of defects is expected to lead to significant band tail states,[47] and poor material quality has been cited as a factor in the relatively low mobilities observed in lateral-transport-based devices. Similarly, it is expected that defects will affect vertical transport by increasing the background current and diminishing or even dominating the NDR peak. However, the exact nature of defects in TMDs is not yet well defined, and full treatment of the variety of band tail states that may be present is complex. For example, band tail states in TMDs are likely due to either vacancies or interstitials, and the capture cross-section of such defects is not well known. To provide an initial understanding of the impact of these states, a simple model was developed in the Supporting Information (Figure S3a and b) to examine the impact of tunneling between states in the conduction and valence bands and defect states in the band gap. It is clear that the presence of significant defect densities will result in much higher background currents and can eliminate the NDR peak. This clearly demonstrates the necessity for higher quality TMD materials for vertical heterostructure applications.

The mechanisms explored in this paper demonstrate that the band structure of the 2D material has important implications for its application to resonant tunneling. Table 1 compares the device performance for TMDs to both conventional resonant tunneling devices and graphene symFETs. Generally, a PVR of 5 or more is necessary for most applications, and for some applications a steep slope with a higher PVR is desirable.[1] The majority of devices contained in the table show low PVRs unsuitable for device applications. Compared to III–V resonant structures, TMD symFETs are not limited by the presence of sub-bands that increase the valley current. While our simulations overestimate the PVR because we include only elastic scattering, theoretical studies of III–V structures restricted to elastic scattering show PVRs at least an order of magnitude below our results for TMD symFETs.[15,17] Graphene-based devices have limited PVR because of a strong dependence of the valley current on the source–drain bias, while the presence of a band edge in TMDs causes a sharp, narrow peak by suppressing the valley current.

Our simulations have important implications for the scaling of symFETs as well. Graphene symFETs require a coherence length of several tens of nanometers for an NDR peak to be present, restricting the minimum device size to approximately this value. In contrast, for MoS_2 symFETs an NDR peak persists to a few nanometers. This means that MoS_2 symFETs could be scaled to meet device size requirements in digital logic applications. Furthermore, the wide range of 2D materials with vastly different properties suggests that an optimized heterostructure could be created out of entirely 2D materials.

CONCLUSIONS

This work demonstrates that the use of TMDs in the symFET architecture has the possibility of drastically improving the achievable PVR over previously considered resonant tunneling devices. In particular, TMD symFETs can produce a PVR up to 10^9, compared to only a few hundred in graphene or III−V RTDs. Additionally, the peak in TMD symFETs will persist to device sizes of only a few nanometers, making these devices highly scalable and appealing for nanoelectronics. However, symFETs fabricated using currently available TMDs are likely to be limited by the presence of band tail states.

METHODS

The charge balance equations relating the oxide voltages, carrier concentrations, and terminal voltages are described in the Supporting Information. For each bias voltage, a Newton−Raphson solver was used to self-consistently solve the charge balance equation and determine the band alignment between the electrodes. Based on the band alignment, the current density was calculated for energies ranging from deep within the valence band to deep within the conduction band. Numerical integration of the current density as a function of energy yielded the total current density for a given bias condition.

Conflict of Interest: The authors declare no competing financial interest.

Supporting Information Available: Simulation of experimental results from ref 26. Detailed explanation of the charge balance and current density equations. Mathematical analysis of the NDR peak position shift at low coherence lengths. The Supporting Information is available free of charge on the ACS Publications website at DOI: 10.1021/nn507174c.

Acknowledgment. This work was supported by the National Science Foundation (through CBET Award 1264705); the Center for Low Energy Systems Technology, one of six centers supported by the STARnet phase of the Focus Center Research Program, a Semiconductor Research Corporation program sponsored by MARCO and DARPA; a Georgia Tech Research Institute Robert G. Shackelford Fellowship (to P.M.C.); and the Swiss National Science Foundation (SNSF) (Grants P2BSP2_148636 and P300P2_158502, to A.T.).

REFERENCES AND NOTES

1. Sun, J. P.; Haddad, G. I.; Mazumder, P.; Schulman, J. N. Resonant Tunneling Diodes: Models and Properties. *Proc. IEEE* **1998**, *86*, 641–661.
2. Esaki, L.; Tsu, R. Superlattice and Negative Differential Conductivity in Semiconductors. *IBM J. Res. Dev.* **1970**, *14*, 61–65.
3. Tsu, R.; Esaki, L. Tunneling in a Finite Superlattice. *Appl. Phys. Lett.* **1973**, *22*, 562–564.
4. Chang, L. L.; Esaki, L.; Tsu, R. Resonant Tunneling in Semiconductor Double Barriers. *Appl. Phys. Lett.* **1974**, *24*, 593–595.
5. Broekaert, T. P. E.; Lee, W.; Fonstad, C. G. Pseudomorphic $In_{0.53}Ga_{0.47}As$/AlAs/InAs Resonant Tunneling Diodes with Peak-to-Valley Current Ratios of 30 at Room Temperature. *Appl. Phys. Lett.* **1988**, *53*, 1545–1547.
6. Ismail, K.; Meyerson, B. S.; Wang, P. J. Electron Resonant Tunneling in Si/SiGe Double Barrier Diodes. *Appl. Phys. Lett.* **1991**, *59*, 973–975.
7. See, P.; Paul, D. J.; Hollander, B.; Mantl, S.; Zozoulenko, I. V.; Berggren, K. F. High Performance $Si/Si_{1-x}Ge_x$ Resonant Tunneling Diodes. *IEEE Electron Device Lett.* **2001**, *22*, 182–184.
8. See, P.; Paul, D. J. The Scaled Performance of $Si/Si_{1-x}Ge_x$ Resonant Tunneling Diodes. *IEEE Electron Device Lett.* **2001**, *22*, 582–584.
9. Luo, L. F.; Beresford, R.; Wang, W. I. Interband Tunneling in Polytype GaSb/AlSb/InAs Heterostructures. *Appl. Phys. Lett.* **1989**, *55*, 2023–2025.
10. Haddad, G. I.; Reddy, U. K.; Sun, J. P.; Mains, R. K. The Bound-State Resonant Tunneling Transistor (BSRTT): Fabrication, D.C. I−V Characteristics and High-Frequency Properties. *Superlattices Microstruct.* **1990**, *7*, 369–374.
11. Capasso, F.; Kiehl, R. A. Resonant Tunneling Transistor with Quantum Well Base and High-Energy Injection: A New Negative Differential Resistance Device. *J. Appl. Phys.* **1985**, *58*, 1366–1368.
12. Reed, M. A.; Frensley, W. R.; Matyi, R. J.; Randall, J. N.; Seabaugh, A. C. Realization of a Three-Terminal Resonant Tunneling Device: The Bipolar Quantum Resonant Tunneling Transistor. *Appl. Phys. Lett.* **1989**, *54*, 1034–1036.
13. Mazumder, P.; Kulkarni, S.; Bhattacharya, M.; Sun, J. P.; Haddad, G. I. Digital Circuit Applications of Resonant Tunneling Devices. *Proc. IEEE* **1998**, *86*, 664–686.
14. Fobelets, K.; VanHoof, C.; Genoe, J.; Stake, J.; Lundgren, L.; Borghs, G. High-Frequency Capacitance of Bipolar Resonant Tunneling Diodes. *J. Appl. Phys.* **1996**, *79*, 905–910.
15. Bowen, R. C.; Klimeck, G.; Lake, R. K.; Frensley, W. R.; Moise, T. Quantitative Simulation of a Resonant Tunneling Diode. *J. Appl. Phys.* **1997**, *81*, 3207–3213.
16. Klimeck, G.; Bowen, R. C.; Boykin, T. B. Off-Zone-Center or Indirect Band-Gap-like Hole Transport in Heterostructures. *Phys. Rev. B* **2001**, *63*, 195310.
17. Sakr, S.; Warde, E.; Tchernycheva, M.; Julien, F. H. Ballistic Transport in GaN/AlGaN Resonant Tunneling Diodes. *J. Appl. Phys.* **2011**, *109*, 023717.
18. Sakuraba, M.; Takahashi, K.; Murota, J. Room-Temperature Resonant Tunneling Diode with High-Ge-Fraction Strained $Si_{1-x}Ge_x$ and Nanometer-Order Ultrathin Si. *ECS Trans.* **2010**, *33*, 379–387.
19. Xia, J. B. Theory of Hole Resonant Tunneling in Quantum-Well Structures. *Phys. Rev. B* **1988**, *38*, 8365–8370.
20. Salvatore, G. A.; Munzenrieder, N.; Barraud, C.; Petti, L.; Zysset, C.; Buthe, L.; Ensslin, K.; Troster, G. Fabrication and Transfer of Flexible Few-Layers MoS_2 Thin Film Transistors to Any Arbitrary Substrate. *ACS Nano* **2013**, *7*, 8809–8815.
21. Yoon, J.; Park, W.; Bae, G. Y.; Kim, Y.; Jang, H. S.; Hyun, Y.; Lim, S. K.; Kahng, Y. H.; Hong, W. K.; Lee, B. H.; *et al.* Highly Flexible and Transparent Multilayer MoS_2 Transistors with Graphene Electrodes. *Small* **2013**, *9*, 3295–3300.
22. Moise, T. S.; Kao, Y. C.; Katz, A. J.; Broekaert, T. P. E.; Celii, F. G. Experimental Sensitivity Analysis of Pseudomorphic InGaAs/AlAs Resonant-Tunneling Diodes. *J. Appl. Phys.* **1995**, *78*, 6305–6317.
23. Zhao, P.; Feenstra, R. M.; Gu, G.; Jena, D. SymFET: A Proposed Symmetric Graphene Tunneling Field-Effect Transistor. *IEEE Trans. Electron Devices* **2013**, *60*, 951–957.
24. Feenstra, R. M.; Jena, D.; Gu, G. Single-Particle Tunneling in Doped Graphene-Insulator-Graphene Junctions. *J. Appl. Phys.* **2012**, *111*, 043711.
25. de la Barrera, S. C.; Gao, Q.; Feenstra, R. M. Theory of Graphene−Insulator−Graphene Tunnel Junctions. *JVST B* **2014**, *32*, 04E101.

26. Britnell, L.; Gorbachev, R. V.; Geim, A. K.; Ponomarenko, L. A.; Mishchenko, A.; Greenaway, M. T.; Fromhold, T. M.; Novoselov, K. S.; Eaves, L. Resonant Tunnelling and Negative Differential Conductance in Graphene Transistors. *Nat. Commun.* **2013**, *4*, 1794.
27. Britnell, L.; Gorbachev, R. V.; Jalil, R.; Belle, B. D.; Schedin, F.; Mishchenko, A.; Georgiou, T.; Katsnelson, M. I.; Eaves, L.; Morozov, S. V.; *et al*. Field-Effect Tunneling Transistor Based on Vertical Graphene Heterostructures. *Science* **2012**, *335*, 947–950.
28. Roy, T.; Liu, L.; de la Barrera, S.; Chakrabarti, B.; Hesabi, Z.; Joiner, C.; Feenstra, R.; Gu, G.; Vogel, E. Tunneling Characteristics in Chemical Vapor Deposited Graphene–Hexagonal Boron Nitride–Graphene Junctions. *Appl. Phys. Lett.* **2014**, *104*, 123506.
29. Mak, K. F.; Lee, C.; Hone, J.; Shan, J.; Heinz, T. F. Atomically Thin MoS_2: A New Direct-Gap Semiconductor. *Phys. Rev. Lett.* **2010**, *105*, 136805.
30. Jariwala, D.; Sangwan, V. K.; Lauhon, L. J.; Marks, T. J.; Hersam, M. C. Emerging Device Applications for Semiconducting Two-Dimensional Transition Metal Dichalcogenides. *ACS Nano* **2014**, *8*, 1102–1120.
31. Wang, Q. H.; Kalantar-Zadeh, K.; Kis, A.; Coleman, J. N.; Strano, M. S. Electronics and Optoelectronics of Two-Dimensional Transition Metal Dichalcogenides. *Nat. Nanotechnol.* **2012**, *7*, 699–712.
32. Najmaei, S.; Liu, Z.; Zhou, W.; Zou, X.; Shi, G.; Lei, S.; Yakobson, B. I.; Idrobo, J.-C.; Ajayan, P. M.; Lou, J. Vapour Phase Growth and Grain Boundary Structure of Molybdenum Disulphide Atomic Layers. *Nat. Mater.* **2013**, *12*, 754–759.
33. Tarasov, A.; Campbell, P. M.; Tsai, M.-Y.; Hesabi, Z. R.; Feirer, J.; Graham, S.; Ready, W. J.; Vogel, E. M. Highly Uniform Trilayer Molybdenum Disulfide for Wafer-Scale Device Fabrication. *Adv. Funct. Mater.* **2014**, *24*, 6389–6400.
34. Tarasov, A.; Zhang, S.; Tsai, M.-Y.; Campbell, P. M.; Graham, S.; Barlow, S.; Marder, S. R.; Vogel, E. M. Controlled Doping of Large-Area Trilayer MoS_2 with Molecular Reductants and Oxidants. *Adv. Mater.* **2015**, *27*, 1175–1181.
35. Li, M.; Esseni, D.; Snider, G.; Jena, D.; Grace Xing, H. Single Particle Transport in Two-Dimensional Heterojunction Interlayer Tunneling Field Effect Transistor. *J. Appl. Phys.* **2014**, *115*.
36. Lam, K. T.; Seol, G.; Guo, J. Operating Principles of Vertical Transistors Based on Monolayer Two-Dimensional Semiconductor Heterojunctions. *Appl. Phys. Lett.* **2014**, *105*.
37. Bardeen, J. Tunnelling from a Many-Particle Point of View. *Phys. Rev. Lett.* **1961**, *6*, 57.
38. Duke, C. B. *Tunneling in Solids*; Academic Press, 1969.
39. Gottlieb, A. D.; Wesoloski, L. Bardeen's Tunnelling Theory as Applied to Scanning Tunnelling Microscopy: A Technical Guide to the Traditional Interpretation. *Nanotechnology* **2006**, *17*, R57.
40. Li, Q. Z.; Hwang, E. H.; Rossi, E.; Das Sarma, S. Theory of 2D Transport in Graphene for Correlated Disorder. *Phys. Rev. Lett.* **2011**, *107*, 156601.
41. Yan, J.; Fuhrer, M. S. Correlated Charged Impurity Scattering in Graphene. *Phys. Rev. Lett.* **2011**, *107*, 206601.
42. Martin, J.; Akerman, N.; Ulbricht, G.; Lohmann, T.; Smet, J. H.; Von Klitzing, K.; Yacoby, A. Observation of Electron-Hole Puddles in Graphene Using a Scanning Single-Electron Transistor. *Nat. Phys.* **2008**, *4*, 144–148.
43. Decker, R.; Wang, Y.; Brar, V. W.; Regan, W.; Tsai, H. Z.; Wu, Q.; Gannett, W.; Zettl, A.; Crommie, M. F. Local Electronic Properties of Graphene on a BN Substrate via Scanning Tunneling Microscopy. *Nano Lett.* **2011**, *11*, 2291–2295.
44. Yankowitz, M.; Xue, J. M.; Cormode, D.; Sanchez-Yamagishi, J. D.; Watanabe, K.; Taniguchi, T.; Jarillo-Herrero, P.; Jacquod, P.; LeRoy, B. J. Emergence of Superlattice Dirac Points in Graphene on Hexagonal Boron Nitride. *Nat. Phys.* **2012**, *8*, 382–386.
45. Xue, J. M.; Sanchez-Yamagishi, J.; Bulmash, D.; Jacquod, P.; Deshpande, A.; Watanabe, K.; Taniguchi, T.; Jarillo-Herrero, P.; Leroy, B. J. Scanning Tunnelling Microscopy and Spectroscopy of Ultra-flat Graphene on Hexagonal Boron Nitride. *Nat. Mater.* **2011**, *10*, 282–285.
46. Goodnick, S. M.; Ferry, D. K.; Wilmsen, C. W.; Liliental, Z.; Fathy, D.; Krivanek, O. L. Surface-Roughness at the Si(100)-SiO_2 Interface. *Phys. Rev. B* **1985**, *32*, 8171–8186.
47. Zhu, W. J.; Low, T.; Lee, Y. H.; Wang, H.; Farmer, D. B.; Kong, J.; Xia, F. N.; Avouris, P. Electronic Transport and Device Prospects of Monolayer Molybdenum Disulphide Grown by Chemical Vapour Deposition. *Nat. Commun.* **2014**, *5*, 3087.